Journal of Materials Chemistry A

ROYAL SOCIETY OF CHEMISTRY

PAPER

View Article Online
View Journal | View Issue

Cite this: J. Mater. Chem. A, 2023, 11, 26164

Neutral d^8 metal complexes with intervalence charge-transfer transition trigger an effective NIR-II photothermal conversion for solar-driven desalination†

Yung-Cong Yang,‡ Joanna S. Lin‡ and Jen-Shyang Ni *

Solar steam generation (SSG) has been a promising solution to water scarcity by evaporating seawater at a low cost and in an eco-friendly way. However, small molecule-based photothermal materials utilized for SSG interfacial layers have been limited owing to their narrow absorption and low solar-thermal conversion. In this work, three neutral d^8 transition-metal (nickel, palladium, and platinum) bis(dithiolene) complexes with an intervalence charge-transfer that induces the second near-infrared (NIR-II) absorption and square-planar geometries favoring intermolecular stacking were synthesized and identified. The metal complex-adsorbed SSG interfacial layer exhibits broad absorption from visible to NIR-II regions for effective solar-light harvesting as well as a high photothermal conversion temperature ranging 155–186 °C under 1064 nm of laser irradiation for 16 s *via* advancing nonradiative heat release. Among them, the best solar energy-to-vapor conversion efficiency of 95.64% and a water evaporation rate of 1.406 kg m^{-2} h^{-1} under one sun irradiation were achieved for nickel complex-based SSG devices. This study provides a strategy for designing solar-thermal conversion materials based on NIR-II organometallic complexes and further successfully advancing them into high-performing solar-driven evaporation applications.

Received 8th September 2023
Accepted 9th November 2023

DOI: 10.1039/d3ta05474h

rsc.li/materials-a

Introduction

The global energy crises and demand for clean water have been two of the great challenges of our modern civilization that have motivated scientists to develop advanced techniques for high-efficiency energy conversion and water purification. Among them, solar steam generation (SSG),[1–4] purifying wastewater or seawater through a solar-thermal conversion interfacial layer, has been regarded as one of the most promising solutions for water purification. The interfacial layer's solar-thermal conversion material (STCM) with broad solar absorption, high photostability, and efficient photothermal conversion has thus been considered a critical factor for improving the solar energy-to-vapor conversion efficiency.[5,6] Thus far, various STCMs with interfacial heat localization, including plasmonic metals,[7,8] carbon-based materials (*e.g.*, graphenes and carbon nanotubes),[9–13] semiconductor-based materials (*e.g.*, metal oxides or sulfides),[14–17] conjugated polymers (*e.g.*, polypyrrole),[6,18–22] and small molecules,[23–25] have been reported for SSG systems with efficient solar-driven water evaporation. Therein, bifunctional solar evaporators, such as metal–organic framework-derived carbon nanoparticle-based evaporators, for simultaneous interfacial solar evaporation and thermoelectric power generation are also current trends in development.[16,17] Furthermore, though STCMs based on organic small molecules have the advantages of structural modification, reproducibility, and fine-tuned optical properties.[26,27] However, they have been rarely developed and utilized in SSG systems because their photobleaching and limited sunlight absorption lead to low solar-thermal conversion efficiency. Accordingly, developing stable small molecule-based STCMs with broad solar absorption is vital for enabling highly efficient solar energy conversion and advancing solar-driven freshwater generation.

The group 10 transition-metal complexes (nickel, palladium, and platinum) based on bis(dithiolene) ligands (Scheme 1) with a diverse range of photophysical properties, such as conductivity, magnetism, and optical properties, have been attractive for applications in the fields of biomedicine, optoelectronics, and materials science.[28–32] For example, the water-soluble pegylated nickel bis(dithiolene) complex with a photothermal conversion efficiency of 12% could induce cell death under the

Department of Chemical and Materials Engineering, Photo-sensitive Material Advanced Research and Technology Center (Photo-SMART), National Kaohsiung University of Science and Technology, Kaohsiung 80778, Taiwan. E-mail: jsni@nkust.edu.tw

† Electronic supplementary information (ESI) available: the detailed synthesis route, ^{1}H and ^{13}C NMR, HRMS, XPS, calculation data, PL spectra in the different mixtures of hexane/ethanol of neutral group-10 metal bis(dithiolene) complexes. See DOI: https://doi.org/10.1039/d3ta05474h

‡ The first two authors have contributed equally to this work.

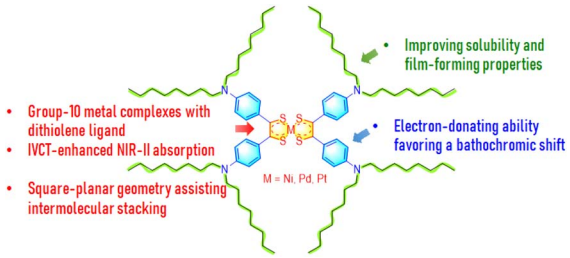

Scheme 1 The design strategy of group 10 transition-metal bis(dithiolene) complexes. IVCT: intervalence charge transfer.

laser irradiation of 940 nm.[28] The biocompatible nickel dithiolene-based polymeric nanoparticles as the photoacoustic (PA) contrast agent have achieved *in vitro* photothermal therapy[31] and *in vivo* deep tissue PA imaging (~5.1 cm)[30] under 1064 nm of laser irradiation. Interestingly, the bis(dithiolene) ligand has been a kind of non-innocent ligand, utilizing a neutral dithioketone, radical monoanion, or dianionic dithiolate to coordinate and form neutral d^8 metal complexes (Scheme S1†).[33–36] Such complexes with a delocalized square-planar electronic structure thus exhibit intense absorption in the near-infrared (NIR) region *via* intervalence charge-transfer (IVCT) transition,[37–39] which makes them potential candidates for solar-driven water evaporation. However, up to now, their absorptions in NIR windows have been quite narrow, leading to difficulty in harvesting sunlight sufficiently. Therefore, we introduced strong electron-donating dialkylamino phenyl substituents into the dithiolene ligand to promote bathochromic absorption as well as effective electron delocalization in coplanar neutral complexes. Moreover, their unique square-planar organometallic center favoring intermolecular stacking in aggregation further extends the absorption spectrum.[34] Interestingly, according to the energy-gap law,[23] the reducing energy gap between the highest occupied molecular orbital (HOMO) and the lowest unoccupied molecular orbital (LUMO) could increase nonradiative decay and release energy *via* heat, which would also be helpful for photothermal conversion properties.[23,26,40–42] As such, strengthening the electronic delocalization and intermolecular stacking in square-planar organometallic complexes is of high importance for amplifying solar absorption and thermal conversion, which will provide insights into the molecular design strategy for new STCMs.

In this work, we rationally designed and synthesized three neutral d^8 complexes (OMCs) with dithiolene ligands and metallic salts *via* one-pot organometallic synthesis route (Scheme 1), in which the dithiolene ligand was derived from the thionation of diketones with phosphorus pentoxide. Compared to traditional organic STCMs, such complexes *via* a coordination reaction were more facile to prepare even though the poor compatibility of reactants in the synthesis resulted in low yields. After that, we investigated their photophysical and photothermal properties *via* experimental measurements supporting our theoretical hypothesis. The results indicated the red-shifting of maximum absorption wavelengths for nickel and palladium complex solutions to the second NIR (NIR-II) region. In contrast, OMC-loading filter papers as the interfacial-heating layer for solar-driven water evaporation can exhibit broad absorption from 300 to 1700 nm, effectively enhancing the sunlight absorption rate. As expected, the intermolecular stacking of OMCs as interfacial-heating evaporation layers can contribute to light harvesting as well as exhibit a high photothermal conversion temperature of 185.5 °C for nickel complex (NiPN) upon 1064 nm laser irradiation for 16 s. This is because square-planar geometries promoting intermolecular stacking in the aggregation and solid states lead to enhanced nonradiative transition decay (heat release) upon excitation, where their radiative processes are thus suppressed. Based on this, the averages of solar energy-to-vapor conversion efficiency and water evaporation rate for NiPN-based SSG devices were evaluated up to 93.02 ± 3.80% and 1.37 ± 0.05 kg m^{-2} h^{-1}, respectively, under one sun light irradiation, which are comparable to the reported materials (Scheme S2†). Freshwater serving as safe drinking water with World Health Organization (WHO) specifications can further be obtained upon solar-driven desalination of seawater. This investigation reveals the molecular design concept and application potential of NIR-II-absorbed organometallic small molecules as STCMs in the highly efficient utilization of solar energy.

Results and discussion

Identification of neutral d^8 metal complexes

The structures and synthetic routes of neutral d^8 transition metal complexes based on the bis(dithiolene) ligand (Scheme S3†) and their molecular characterizations are included in the ESI† and Fig. 1. Compared to $(Oct_2NPhCO)_2$ of dithiolene precursor, the ^1H NMR peaks of phenyl ring around the organometallic center are upfield shifting with the increasing heavy atom effect (Fig. 1a), with 7.34, 7.27, and 7.25 ppm for NiPN, PdPN, and PtPN, respectively. Their ^{13}C NMR peaks of the dithiolene ligand also shifted from 179.01 (NiPN) and 179.76 ppm (PdPN) to 175.52 ppm (PtPN) (Fig. S2, S5, and S8†).

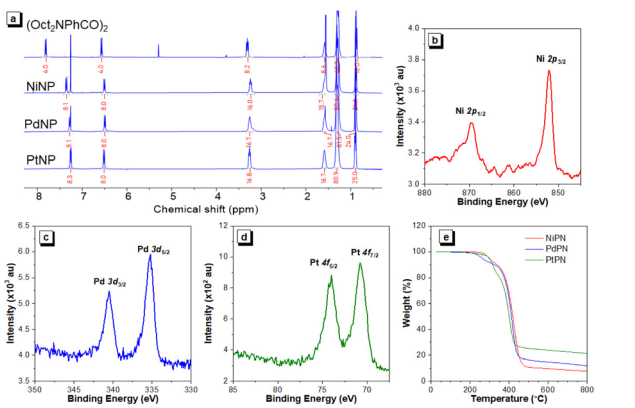

Fig. 1 Structural identification and thermal stability. (a) ^1H NMR spectra of NIR-II organometallic complexes (OMCs) and dithiolene precursor $(Oct_2NPhCO)_2$. X-ray photoelectron spectroscopy (XPS) analysis of (b) NiPN, (c) PdPN, and (d) PtPN. (e) The thermogravimetric analysis (TGA) of OMCs.

For X-ray photoelectron spectroscopy (XPS) (Fig. 1b–d and S10†), the signals of S 2p (163 eV), N 1s (396 eV), Ni (851, 869 eV), Pd (336, 341 eV), and Pt (71, 74 eV) respectively reveal their elemental composition as well as the chemical and electronic state of the atoms within the complexes. The thermogravimetric analysis (TGA) shows good thermal stability temperatures (Fig. 1e), where the unburned remaining weights heated over 400 °C could be considered the central metal wreck. Herein, the identification experiments verify the chemical structures and thermal stability of neutral group-10 metal complexes with the bis(dithiolene) ligand.

Optical properties of neutral d^8 metal complexes

In terms of photophysical measurement, the UV-vis-NIR absorption spectra of the OMCs measured in hexane solution (10 μM) at room temperature display a strong absorption band in the NIR region (Fig. 2a). The maximum absorption wavelengths of 1054, 1067, and 984 nm for NiPN, PdPN, and PtPN, respectively, are attributed to the IVCT transition of the delocalized ligand system.[37] Those in visible absorption bands originate from the ligand-to-metal charge transfer and intense π–π* transitions.[37,43] Upon excitation at 808 nm, they emitted in the NIR-II region, whose maximum wavelengths are 1150, 1115, and 1102 nm for NiPN, PdPN, and PtPN, respectively (Fig. 2b). The highly fluorescent intensity for PdPN may result from low reorganization energy and nonadiabatic decay of the deexcitation process and its heavy-atom effect on the central metal.[44,45] Similarly, the apparently solvatochromic emission for PdPN is confirmed from the Lippert–Mataga plots of Stokes shifts *versus* the solvent orientation polarizability (Fig. 2c and S11†).[46] To gain insights into the photophysical properties of OMCs in the aggregation state, their fluorescent properties were further investigated in hexane and hexane/ethanol mixtures with different ethanol fractions (Fig. S12–S14†). With the increase in the poor solvent (ethanol) proportion, PdPN shows apparent aggregation-caused fluorescence diminishing phenomena (Fig. 2d), while the fluorescent intensities of NiPN and PtPN are still relatively weak. This implies that the excited OMCs in the aggregation state mainly release energy through nonradiative decay, such as heat, not the radiative process.[44] However, as aggregated, the square-planar molecular geometries decrease the intermolecular distance and strengthen π–π interactions, driving aggregation-caused quenching fluorescence, *i.e.*, the aggregation-enhanced nonradiative energy release and photothermal conversion performance upon irradiation (*vide infra*).

As expected, under NIR-II laser irradiation (1064 nm, 1 W cm^{-2}) for 15 min, the temperature of OMC aggregates (100 μg mL^{-1} in deionized water) can rise up to 41.2 °C (NiPN), 34.5 °C (PdPN), and 38.7 °C (PtPN), respectively (Fig. 2e). The photothermal conversion efficiencies (PTCEs) were then calculated to be 42.3%, 17.1%, and 18.4% for NiPN, PdPN and PtPN, respectively. To understand the actual photothermal property of the solar-to-vapor interfacial layer based on OMCs, the photothermal conversion temperatures for filter paper-adsorbed OMCs were further measured under NIR-II laser irradiation (1064 nm, 1 W cm^{-2}). As shown in Fig. 2f, the temperatures upon irradiation for 16 s are sharply rising to 185.5 °C (NiPN), 154.8 °C (PdPN), and 166.5 °C (PtPN), respectively, whereas that of blank filter-paper does not obviously change (33.8 °C). Besides, the filter paper-adsorbed commercial activated carbon with UV-vis-NIR absorption shows 132.6 °C upon irradiation. This suggests that NIR-II OMC-loaded filter papers can efficiently convert laser into heat energies and be suitable for an interfacial layer to generate evaporation freshwater (*vide infra*).

Theoretical calculations of neutral d^8 metal complexes

To understand their photophysical properties, theoretical calculations for ground (S_0) and excited (S_1) states of OMCs were carried out with a time-dependent density functional theory

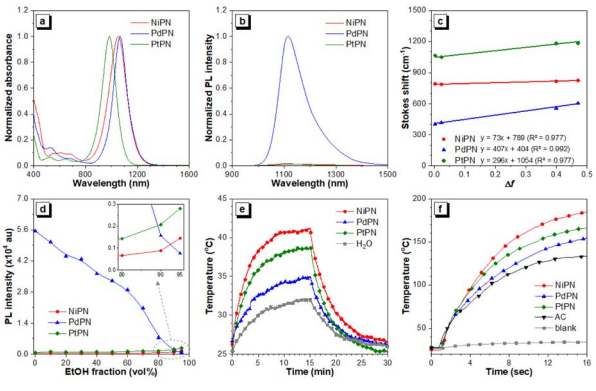

Fig. 2 The photophysical and photothermal properties of NIR-II OMCs. (a) Normalized UV-vis-NIR absorption and (b) photoluminescence (PL) spectra in hexane (10 μM). (c) Lippert–Mataga plots of Stokes shifts *versus* the solvent orientation polarizability (10 μM). (d) PL intensity changes with the increase in ethanol (EtOH) fraction in hexane/EtOH mixtures. Time-dependent temperature changes of deionized water (H_2O) and OMCs (100 μg mL^{-1}) in H_2O (e) and OMCs and activated carbon (AC) adsorbed onto the filter paper (f), respectively, under the laser irradiation of 1064 nm (1 W cm^{-2}).

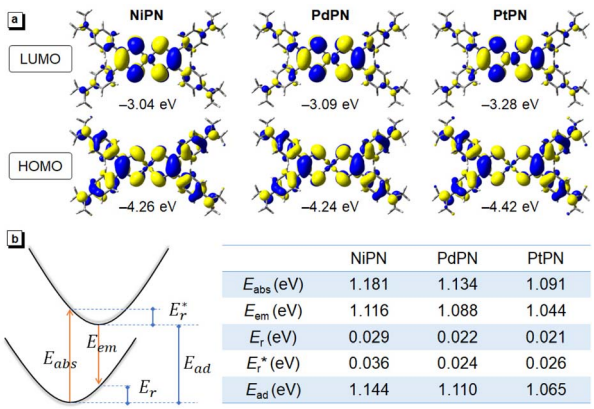

	NiPN	PdPN	PtPN
E_{abs} (eV)	1.181	1.134	1.091
E_{em} (eV)	1.116	1.088	1.044
E_r (eV)	0.029	0.022	0.021
E_r^* (eV)	0.036	0.024	0.026
E_{ad} (eV)	1.144	1.110	1.065

Fig. 3 Theoretical calculations of NIR-II OMCs. (a) The electron cloud distribution of the HOMO and LUMO with an isovalue of 0.02 au and their energy levels. (b) A schematic diagram of energy levels and their relative energy. E_{abs}, E_{em}, E_r, E_r^*, and E_{ad} denote the energy difference of absorption from S_0 to S_1 states, that of emission from S_1 to S_0 states, that of relaxation in the S_0 state, that of relaxation in the S_1 state, and that between the minimum S_1 and S_0 states, respectively.

(TD-DFT) at the level of B3LYP/6-31G(d)/LANL2DZ. As shown in Fig. 3, S15–S17, Tables S1 and S2,† the optimized molecular geometries observe square-planar bis(dithiolene) complexes associated with typically d^8 transition-metal cations (Ni^{2+}, Pd^{2+}, and Pt^{2+}), which is beneficial for intermolecular stacking in aggregation or solid states and further extending absorption to NIR-II window (*vide infra*). The electron densities of HOMO are distributed from the electron-donating aminophenyl-substituent to organometallic complexes. By contrast, those of LUMO are concentrated on the metal dithiolene central, in which some electronic clouds can extend out onto the pendent phenyl-rings as well. Therefore, the energy levels of LUMO are evidently down-shifted from −3.04 eV (NiPN) to −3.20 eV (PdPN) and −3.28 eV (PtPN) due to the heavy atom effect of central metal. This also causes narrowed energy gaps and decreased adiabatic energies (E_{ad}) as central metals are exchanged from nickel to palladium and platinum. According to the analysis of the four-point method,[47] the energy difference of absorption from S_0 to S_1 states (E_{abs}), that of emission from S_1 to S_0 states (E_{em}), that of relaxation in the S_0 (E_r) and S_1 (E_r^*) states, and E_{ad} were estimated, respectively, and they are listed in the table of Fig. 3b. The narrowing E_{abs} and E_{em} values are attributed to the heavy atom effect of central metal from nickel exchanged to palladium and platinum, which corresponds with the experiment results (*vide supra*). In addition, the E_r^* and E_r values caused by vibrational relaxation mean the configurational reorganization energies between S_0 and S_1 states, which are a leading cause of the nonradiative transition decay.[46,47] The total reorganization energies ($E_r^* + E_r$ values) for NiPN (65 meV) are higher than those for PdPN (46 meV) and PtPN (47 meV), implying more considerable vibrational relaxation energy for the former in deexcitation. The configurational reorganization *via* the nonradiative decay will favor enhancing the photothermal conversion property.[44] As such, this result explains NiPN displaying dim emission and high photothermal temperature and further supports it as a STCM for SSG application.

Optical properties and wettability of NiPN-based interfacial layer

Based on the good photothermal performance of the bis(dithiolene)-coordinated nickel complex, we first evaluated the effect of the NiPN-adsorbed metering on the solar energy-to-vapor interfacial layer. The filter papers were coated with different amounts (1.25, 2.5, 5.0, 10.0, and 15.0 mg) of NiPN complex, forming OMC-loading interfacial-heating evaporation layers (OMC layers). As observed from the UV-vis-NIR reflection-absorption spectra (Fig. 4a), all absorption wavelengths from 300 to 1700 nm are similar and reach the maximum absorbance after loading over 5 mg of NiPN materials. This indicates that the optimal usage of materials is about 5 mg on the filter paper with a diameter of 2 cm. Furthermore, no or dim emissions for OMC layers (Fig. S18†) suggest that the nonradiative decay, such as heat, is the primary energy release upon deexcitation. To evaluate the applicability of the SSG system, the water contact angles (WCAs) were measured to analyze OMC layers' wettability

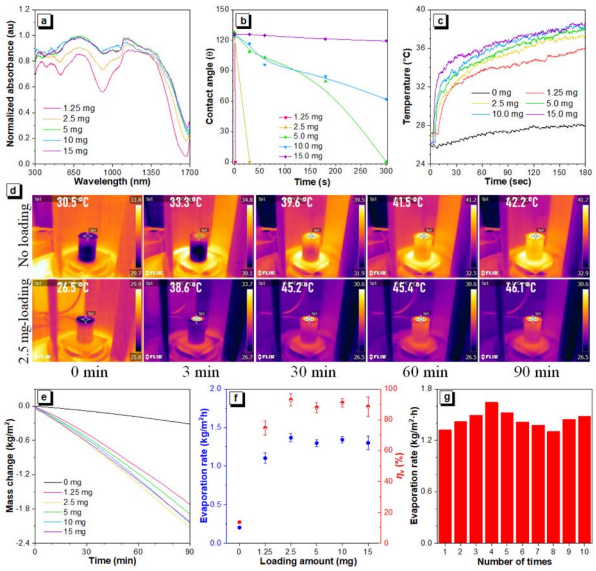

Fig. 4 The photophysical properties of and solar-steam generation (SSG) by NiPN-based films. (a) Reflective UV-vis-NIR absorption spectra, (b) time-dependent contact angles, (c) time-dependent temperature changes, (d) infrared images of the solar-thermal interfacial-heating evaporation layers, and (e) water-mass change curves under one sun irradiation for NIR-II films with different amounts of NiPN-loading. (f) The relationship between the evaporation rate (blue) and the solar energy-to-vapor conversion efficiency (η_v; red) for the different loading amounts of NiPN under one sun irradiation. (g) The SSG stability for 2.5 mg of NiPN-loading device.

(Fig. S19 and S20†). Based on time-dependent contact angles (Fig. 4b), the waters for 1.25 and 2.5 mg of OMC layers spread completely within about 9 and 30 s after water dropping, respectively, whereas that for 5 mg of OMC layers also flattened after 5 min (Fig. S20†). By comparison, after water-dropping for *ca.* 5 min, the WCAs are 61.8° and 119.1° for 10 and 15 mg of OMC layers (Fig. S20†), respectively. This indicates that the void of filter papers will be hydrophilized after loading with excessive hydrophobic NiPN materials, weakening the surface hydrophilicity. However, the hydrophilic photothermal surface will be relatively suitable for water vapor penetration upon irradiation using a solar simulator. We thus reasonably speculate that the 2.5 mg of OMC-loading layer with high UV-vis-NIR absorbance and suitable hydrophilicity should display the best solar-driven evaporation system.

Solar-thermal conversion properties of the NiPN-based SSG system

To determine the influence of the NiPN-adsorption amounts on the solar energy-to-vapor conversion efficiency, the OMC layers of the solar energy-to-vapor conversion devices were fabricated for SSG measurement (Fig. S21†), in which blank filter paper without any NiPN loading was used as the reference. As shown in Fig. 4c, d and S22,† after solar irradiation over 3 min, the equilibrium temperature of the OMC layers' surfaces increases in the order of 1.25 (36.1 °C), 2.5 (37.5 °C), 5.0 (38.5 °C), 10.0 (38.6 °C), and 15.0 mg (39.0 °C) of NiPN-loading amounts. This

result is in proportion to the increasing mass loading and absorbance. By contrast, the temperature slightly increases only (ΔT ~2.1 °C) for the blank filter paper without OMC loading. To further assess the efficiency of solar-driven water evaporation, the typical curves of time-dependent water-mass change under solar irradiation (1 sun, 1 kW m^{-2}) were measured with the simulated setup displayed in real time and *in situ* (Fig. S21†). The deionized water evaporation rate ($\dot{m}$) from the slope of time-dependent water-mass change curves (Fig. 4e) increases to be as high as 1.37 ± 0.05 kg m^{-2} h^{-1} for 2.5 mg of NiPN adsorbed, compared to the other metered OMC layers (1.10 ± 0.07 kg m^{-2} h^{-1} for 1.25 mg, 1.30 ± 0.05 kg m^{-2} h^{-1} for 5.0 mg, 1.34 ± 0.04 kg m^{-2} h^{-1} for 10.0 mg, and 1.30 ± 0.09 kg m^{-2} h^{-1} for 15.0 mg). Compared with the blank filter paper, only 0.20 ± 0.01 kg m^{-2} h^{-1} of $\dot{m}$ value, water evaporation using OMC layers is greatly accelerated. Herein, the solar energy-to-vapor conversion efficiency (η_v) for 2.5 mg of NiPN-adsorbed film is as high as 93.02 ± 3.80% compared to that for the other OMC layers (Fig. 4f), 74.72 ± 4.64% for 1.25 mg, 88.02 ± 3.20 for 5.0 mg, 91.16 ± 2.81 for 10.0 mg, and 88.60 ± 6.19 for 15.0 mg, respectively.[23] The blank filter paper as a solar evaporator behaves with the lowest η_v value of 13.65 ± 0.61%. Under the same conditions, 2.5 mg of activated carbon-adsorbed evaporator exhibits 1.256 kg m^{-2} h^{-1} of water evaporation rate with 85.7% efficiency (Fig. S23†).[48] After optimization, the best water-mass change and solar energy-to-vapor conversion efficiency for 2.5 mg of OMC layer can be achieved at 1.406 kg m^{-2} h^{-1} and 95.64%, respectively, for the NiNP-adsorbed SSG system. The NiNP-adsorbed evaporator exhibits 0.19 W m^{-1} K^{-1} of thermal conductivity and 32.1% of heat loss.[17,49] Additionally, its evaporation rate is also stable after seven cycles (Fig. 4g), indicating that the NiPN-adsorbed film can efficiently and stably convert sunlight into heat and exhibit excellent SSG performance.

To explore the relationship between incident-light intensity and evaporation rate and efficiency, SSG devices based on 2.5 mg of OMC layer under different sunlight intensities (2 and 3 suns) were further investigated, as shown in Fig. 5a–d. The surface temperature of the NiPN-adsorbed film rises rapidly to 43.6 °C under 2-sun irradiation, and to 47.3 °C under 3-sun irradiation within 3 min (Fig. 5a and d). The $\dot{m}$ values are 2.11 ± 0.03 and 3.17 ± 0.04 kg m^{-2} h^{-1} under irradiation of 2 and 3 suns (Fig. 5b), respectively, and the evaporation efficiency was calculated to be 71.98 ± 0.96% for 2-sun and 72.01 ± 0.86% for 3-sun irradiation (Fig. 5c). Despite the growing $\dot{m}$ values with the increase in power intensities, the results show optimum SSG performance for the NiPN-adsorbed evaporation interface layer under irradiation of one sunlight.

Solar-driven desalination of the NiPN-based SSG system

In efforts to resolve water shortages across the globe, developing efficient and green seawater desalinization approaches is of great importance to overcome the complicated preparation process and equipment costs of traditional ones. Hence, the deionized water was changed to Sizihwan seawater (Taiwan) to assess the desalination ability of the SSG system based on the NiPN-adsorbed evaporator. As shown in Fig. 6a, the water-mass change in seawater under 1-sun irradiation for 90 min is close to that in deionized water. The best $\dot{m}$ value in seawater is 1.38 kg m^{-2} h^{-1} (an average of 1.34 ± 0.04 kg m^{-2} h^{-1}), converting to 93.05% of the evaporation efficiency (an average of 90.18 ± 2.87%). Compared with the SSG results of deionized water, the slightly decreasing efficiency of about 3% for seawater evaporation may be owing to the salt crystals appearing on the solar energy-to-vapor interface layer. In the process of solar-steam

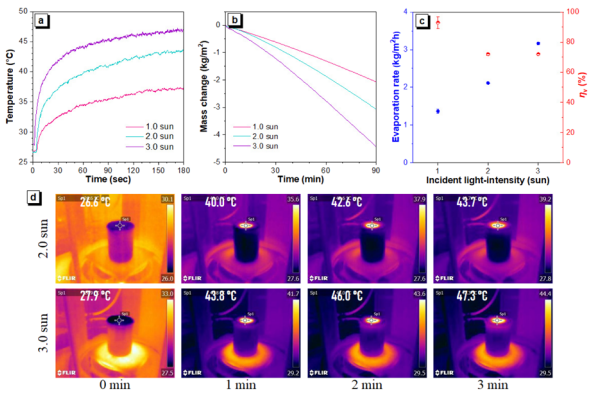

Fig. 5 The lighting intensity test and desalination application of NiPN-based films. Time-dependent temperature changes (a) and water-mass change curves (b), and (c) the relationship between the evaporation rate (blue) and the solar energy-to-vapor conversion efficiency (η_v; red) for 2.5 mg of NiPN-loading device under different solar irradiations. (d) Infrared images of the solar-thermal interfacial-heating evaporation layers under 2.0 and 3.0 sun irradiation.

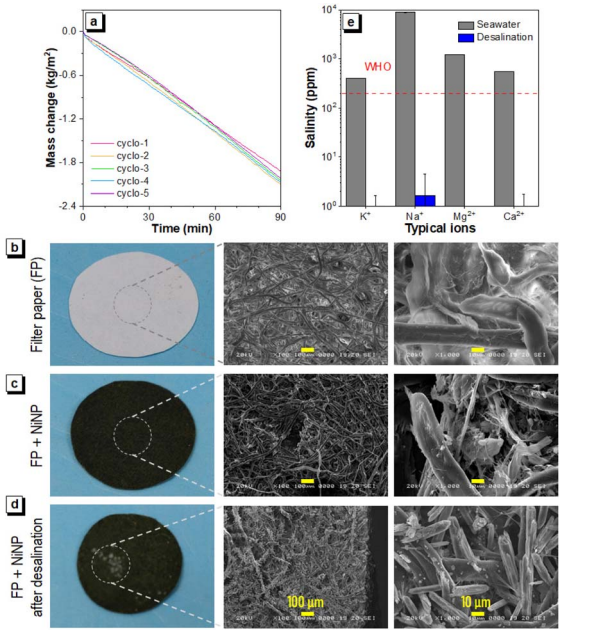

Fig. 6 The desalination application of NiPN-based films. (a) Time-dependent water-mass change curves for Sizihwan seawater evaporation using 2.5 mg of the NiPN-loading device under one sun irradiation. Scanning electron microscopy (SEM) images of the (b) blank filter paper (FP), (c) NiPN loading FP, and (d) NiPN-adsorbed FP after desalination. (e) Four ion concentrations of the seawater before and after desalination.

desalination, the vapor escape from the filter paper causes the surface's sea-salt deposition, which will hinder the water vapor from passing through the pores of the NiNP-adsorbed evaporator. In view of this, scanning electron microscope (SEM) analysis was further used to visualize interface layers' surface features. As shown in Fig. 6b, blank filter paper shows a smooth fiber surface, whereas that based on the NiPN complex displays rough and even partial aggregation (Fig. 6c). Upon desalination with 5 sun irradiation, salt crystals appearing and spreading over the fiber surface of filter paper can be clearly noticed with SEM images (Fig. 6d and S24†). Herein, the salt precipitation on the OMC-evaporator will hinder the evaporation of seawater and thus bring about declining SSG efficiency during the desalination process of the actual seawater. To overcome this problem in the future, we will combine photothermal materials with the water-absorbency porous supporter with capillary action and super-hydrophilic wettability to construct the evaporator, which may exhibit excellent salt-resistant performance through dissolving sea salt above the solar evaporator.[20]

After that, four primary ion concentrations of natural seawater (K^+, Na^+, Ca^{2+}, and Mg^{2+}) before and after desalination were analyzed by inductively coupled plasma optical emission spectrometry (ICP-OES), and their results are shown in Fig. 6e, where Sizihwan seawater contains 407 ppm of K^+, 8917 ppm of Na^+, 553 ppm of Ca^{2+}, and 1223 ppm of Mg^{2+} ions, respectively. After solar-driven seawater evaporation, it can be clearly seen that ion concentrations (1.0 ppm of K^+, 1.7 ppm of Na^+, 0.9 ppm of Ca^{2+}, and 0.4 ppm of Mg^{2+} ions) reduce significantly in freshwater, which is far below the WHO standard for safe drinking water ion concentrations. These results reveal that solar evaporator based on the NiPN-adsorbed SSG interfacial layer has the same excellent evaporation performance in seawater. In other words, the NIR-II OMC-loading filter paper as a solar-thermal absorber for the SSG system is a potential application to produce freshwater by solar-driven seawater evaporation.

Conclusions

This work proposed three neutral d^8 metal bis(dithiolene) complexes with strong electron-donating substituents to develop high-performance light absorbers. The broad UV-vis-NIR absorbed behaviors from 300 to 1700 nm for efficient sunlight harvesting are attributed to the synergistic effect of IVCT transition and intermolecular stacking. Among them, the nickel complex (NiPN) with high reorganization energy caused dim emission and high PTCE is suitable for serving as a STCM for water evaporation. The NiPN-loading interfacial layer has also proven to be the best candidate for solar-driven evaporators with a water-mass evaporation rate of 1.406 kg m^{-2} h^{-1} and a solar energy-to-vapor conversion efficiency of 95.64% under one sun simulated solar irradiation. As a result, this STCM exhibits excellent performance in seawater desalination and then obtained freshwater by WHO standards. Compared to organic small molecule-based STCM, a neutral nickel bis(dithiolene) complex tying electron-donating substituent exhibits a broader range of UV-vis-NIR absorption for effective solar-light harvesting and higher photothermal conversion temperature (185.5 °C for 16 s, 1064 nm irradiation) for accelerating water evaporation. Thus, the SSG system based on a NiNP-adsorbed evaporator has certain competitive advantages of solar energy-to-thermal water evaporation rate and efficiency. This investigative elucidation will not only successfully apply NIR-II absorbed organometallic complexes in solar-heating water evaporation but also assist in expanding new STCMs for sustainable and green water treatment development.

Experimental section

Materials and methods

Chemicals were purchased from Sigma-Aldrich and TCI and used directly without further purification. Tetrahydrofuran (THF) was distilled from sodium benzophenone ketyl under a dry Ar flow immediately before use. Other solvents were directly used without further purification. ^{1}H and ^{13}C NMR spectra were recorded using a Varian VNMRS 600 MHz spectrometer with $CDCl_3$ as the solvent and tetramethylsilane (TMS) as the internal standard. High-resolution mass spectra (HRMS) were recorded using an Autoflex Speed Bruker, operating in a MALDI-TOF mode. UV-vis-NIR absorption and photoluminescence (PL) spectra were recorded using a ProTrusTech spectrometer with an Avantes' SensLine and MRID, respectively. The thermogravimetric analysis (TGA) was recorded using a Mettler-Toledo spectrometer at a heating rate of 20 °C min^{-1}. The contact angle was measured using an OSA 60, NBSI. The scanning electron microscopy (SEM) image was acquired using a JSM-5610, JEOL. The inductively coupled plasma optical emission spectrometry (ICP-OES) was performed using an iCAP 7000 Series, Thermo Scientific.

Synthesis of neutral d^8 metal bis-dithiolene complexes

1,2-Bis[4-(di-*n*-octylamino)phenyl]ethane-1,2-dione (1.9 equiv.) and phosphorus pentasulfide (P_2S_5; 4.7 equiv.) dissolved in 1,3-dimethyl-2-imidazo-lidinone (DMI; 0.1 M) were heated at 95 °C for 10 h. A solution of "salt" (1 equiv.) in distilled water (0.4 M) was added to the mixtures and further heated at 90 °C for 4 h. After cooling, the solution is poured into distilled water and extracted thrice with dichloromethane (CH_2Cl_2). The combined organic fractions were dried over anhydrous $MgSO_4$ and concentrated *via* rotary evaporation. The residue was purified by column chromatography using silica gel and CH_2Cl_2/hexanes (1/4, v/v) as the eluent to give a solid.

NiPN. Dark-green solid, 66.10% of yield. ^{1}H NMR (400 MHz, $CDCl_3$), δ (ppm): 7.344 (d, J = 8.8 Hz, 8H), 6.516 (d, J = 8.8 Hz, H), 3.240 (m, 16H), 1.56 (m, 16H), 1.308 (m, 80H), 0.887 (m, 24H). ^{13}C NMR (400 MHz, $CDCl_3$), δ (ppm): 179.007, 148.536, 130.399, 130.002, 110.846, 51.130, 31.813, 29.474, 29.323, 27.261, 27.160. 22.639, 14.093. HRMS (MALDI-TOF): calculated for $C_{92}H_{152}N_4NiS_4$ $[M]^+$ 1501.1894; found: 1501.0180.

PdPN. Dark-brown viscous liquid, 15.83% of yield. ^{1}H NMR (400 MHz, $CDCl_3$), δ (ppm): 7.266 (d, J = 8.8 Hz, 8H), 6.506 (d, J = 8.8 Hz, H), 3.258 (m, 16H), 1.571 (m, 16H), 1.311 (m, 80H), 0.894 (m, 24H). ^{13}C NMR (400 MHz, $CDCl_3$), δ (ppm): 179.761,

148.674, 131.087, 130.596, 110.663, 51.079, 31.795, 29.451, 29.303, 27.301, 27.131, 22.621, 14.077. HRMS (MALDI-TOF): calculated for $C_{92}H_{152}N_4PdS_4$ $[M]^+$ 1546.9935; found: 1546.9977.

PtPN. Dark-green solid, 15.32% of yield. ^{1}H NMR (400 MHz, $CDCl_3$), δ (ppm): 7.248 (d, J = 8.4 Hz, 8H), 6.524 (d, J = 8.8 Hz, H), 3.262 (m, 16H), 1.589 (m, 16H), 1.316 (m, 80H), 0.896 (m, 24H). ^{13}C NMR (400 MHz, $CDCl_3$), δ (ppm): 175.515, 148.456, 130.264, 129.715, 110.837, 51.059, 31.811, 29.474, 29.321, 27.315, 27.158, 22.634, 14.085. HRMS (MALDI-TOF): calculated for $C_{92}H_{152}N_4PtS_4$ $[MH]^+$ 1637.0626; found: 1637.0490.

Theoretical calculations

The optimized geometries of the ground-state (S_0) and excited-state (S_1) minima were calculated using Gaussian 16 with time-dependent density functional theory (TD-DFT) at the level of B3LYP using the Gauss View 6 software.[50] All non-metallic atoms (C, H, S, and N) and metal atoms (Ni, Pd, and Pt) were located *via* a combined basis set of 6-31G(d) and LANL2DZ, respectively.

Solar steam generation (SSG) measurements

The solar energy-to-vapor conversion efficiency (η_v) in solar-steam generation devices was calculated using the following equation:[23]

$$\eta_v = \frac{\dot{m} h_{LV}}{C_{opt} P_0}$$

where $\dot{m}$ refers to the water mass flux (evaporation rate), C_{opt} represents the optical concentration, and P_0 is the nominal solar irradiation value of the sunlight intensity, respectively. h_{LV} refers to the total liquid–vapor phase-change enthalpy, *i.e.*, the sensible heat and the enthalpy of vaporization, in the following formula:

$$h_{LV} = Q + \Delta h_{vap}$$

where Q is the energy provided to heat the system from the initial ambient temperature (T_0) to the final absorber's temperature (T_{abs}), and Δh_{vap} is the latent heat of water vaporization.

The heat loss efficiencies of conduction (η_{cond}), radiation (η_{rad}), and convection (η_{conv}) for the device can be estimated using the following equations:[17,49]

$$\eta_{cond} = \frac{C_w \cdot m \cdot \Delta T / A \cdot t}{P_0} = \frac{h_{cond}(T_u - T_b)/d}{P_0}$$

$$\eta_{rad} = \varepsilon\sigma({T_{abs}}^4 - {T_0}^4)/P_0$$

$$\eta_{conv} = h_{conv}(T_{abs} - T_0)/P_0$$

where C_w is the specific heat capacity of liquid water (4.2 J g^{-1} K^{-1}), m is the water mass, ΔT is the temperature change before and after SSG, A is the evaporation surface area, h_{cond} is the thermal conductivity of the wetted absorber (W m^{-1} K^{-1}), d is the thickness of the insulator, T_u and T_b are the temperatures of the upper and bottom layers of the insulator, respectively, ε is the effective thermal emissivity of the absorber, σ is the Stefan–Boltzmann constant (5.67 $\times$ 10^{-8} W m^{-2} K^{-4}), and h_{conv} is the convective heat transfer coefficient (5 W m^{-2} K^{-1}).

Conflicts of interest

There are no conflicts to declare.

Acknowledgements

We are grateful for financial support from National Science and Technology Council (NSTC 111-2113-M-992-001-MY2, Taiwan) and theoretical calculation support from National Center for High-Performance Computing (NCHC, Taiwan).

Notes and references

1 W. Shang and T. Deng, Solar steam generation: Steam by thermal concentration, *Nat. Energy*, 2016, **1**, 16133.
2 P. Tao, G. Ni, C. Song, W. Shang, J. Wu, J. Zhu, G. Chen and T. Deng, Solar-driven interfacial evaporation, *Nat. Energy*, 2018, **3**, 1031–1041.
3 L. Wang, Y. Feng, K. Wang and G. Liu, Solar water sterilization enabled by photothermal nanomaterials, *Nano Energy*, 2021, **87**, 106158.
4 I. Ibrahim, D. H. Seo, A. M. McDonagh, H. K. Shon and L. Tijing, Semiconductor photothermal materials enabling efficient solar steam generation toward desalination and wastewater treatment, *Desalination*, 2021, **500**, 114853.
5 V. Kashyap and H. Ghasemi, Solar heat localization: Concept and emerging applications, *J. Mater. Chem. A*, 2020, **8**, 7035–7065.
6 S. Cao, A. Thomas and C. Li, Emerging materials for interfacial solar-driven water purification, *Angew. Chem., Int. Ed.*, 2023, **62**, e202214391.
7 Z. Huang, S. Li, X. Cui, Y. Wan, Y. Xiao, S. Tian, H. Wang, X. Li, Q. Zhao and C.-S. Lee, A broadband aggregation-independent plasmonic absorber for highly efficient solar steam generation, *J. Mater. Chem. A*, 2020, **8**, 10742–10746.
8 Y. Zhang, Y. Wang, B. Yu, K. Yin and Z. Zhang, Hierarchically structured black gold film with ultrahigh porosity for solar steam generation, *Adv. Mater.*, 2022, **34**, e2200108.
9 X. Li, Y. Tian, P. Zhang, N. Liu, H. Zhai, J. Ji, S. Zhao, Y. Liu, D. Xu, F. Wang, Y. Wei and L. Feng, A lotus-petiole-inspired hierarchical design with hydrophilic/hydrophobic management for enhanced solar water purification, *Adv. Funct. Mater.*, 2023, **33**, 2302019.
10 W. M. Zhang, J. Yan, Q. Su, J. Han and J. F. Gao, Hydrophobic and porous carbon nanofiber membrane for high performance solar-driven interfacial evaporation with excellent salt resistance, *J. Colloid Interface Sci.*, 2022, **612**, 66–75.
11 N. T. Nhat Hang, N. Van Canh, N. H. Hoa, P. D. Du, P. H. Le and V. Nguyen, Co-assembled hybrid of carbon nanodots and molecular fluorophores for efficient solar-driven water evaporation, *Carbon*, 2022, **199**, 462–468.

12 T. Arunkumar, H. W. Lim, D. Denkenberger and S. J. Lee, A review on carbonized natural green flora for solar desalination, *Renewable Sustainable Energy Rev.*, 2022, **158**, 112121.
13 N. Liu, L. Hao, B. Zhang, R. Niu, J. Gong and T. Tang, Rational design of high-performance bilayer solar evaporator by using waste polyester-derived porous carbon-coated wood, *Energy Environ. Mater.*, 2021, **5**, 617–626.
14 S. Ai, M. Ma, Y.-Z. Chen, X.-H. Gao and G. Liu, Metal-ceramic carbide integrated solar-driven evaporation device based on ZrC nanoparticles for water evaporation and desalination, *Chem. Eng. J.*, 2022, **429**, 132014.
15 Z. Guo, W. Zhou, N. Arshad, Z. Zhang, D. Yan, M. S. Irshad, L. Yu and X. Wang, Excellent energy capture of hierarchical MoS_2 nanosheets coupled with mxene for efficient solar evaporators and thermal packs, *Carbon*, 2022, **186**, 19–27.
16 Z. Fan, J. Ren, H. Bai, P. He, L. Hao, N. Liu, B. Chen, R. Niu and J. Gong, Shape-controlled fabrication of MnO/C hybrid nanoparticle from waste polyester for solar evaporation and thermoelectricity generation, *Chem. Eng. J.*, 2023, **451**, 138534.
17 P. He, H. Bai, Z. Fan, L. Hao, N. Liu, B. Chen, R. Niu and J. Gong, Controllable synthesis of N/Co-doped carbon from metal–organic frameworks for integrated solar vapor generation and advanced oxidation processes, *J. Mater. Chem. A*, 2022, **10**, 13378–13392.
18 Y. Li, S. Zhang, Z. Xia, L. Wang and J. Fan, Micro-macro-capillaries fabric-based evaporator for eliminating salt accumulation and highly efficient solar steam generation, *Sep. Purif. Technol.*, 2023, **308**, 122852.
19 X. Yan, S. Lyu, X. Q. Xu, W. Chen, P. Shang, Z. Yang, G. Zhang, W. Chen, Y. Wang and L. Chen, Superhydrophilic 2D covalent organic frameworks as broadband absorbers for efficient solar steam generation, *Angew. Chem., Int. Ed.*, 2022, **61**, e202201900.
20 S. Wang, Y. Fan, F. Wang, Y. Su, X. Zhou, Z. Zhu, H. Sun, W. Liang and A. Li, Potentially scalable fabrication of salt-rejection evaporator based on electrogenerated polypyrrole-coated nickel foam for efficient solar steam generation, *Desalination*, 2021, **505**, 114982.
21 T. T. Pham, M. T. Nguyen, H. G. Nguyen, T. A. H. Nguyen, D. B. Do, D. C. Nguyen, D. Tanaka and D. D. Nguyen, Fe(III)-natural polyphenols bilayer coatings on fingered citron as a novel photothermal material for sustainable seawater desalination, *Desalination*, 2022, **537**, 115873.
22 S. Q. Li, Y. Deng, J. Huang, P. Wang, G. Liu and H. L. Xie, Light-absorbing copolymers of polyimides as efficient photothermal materials for solar water evaporation, *Aggregate*, 2023, **4**, e371.
23 G. Chen, J. Sun, Q. Peng, Q. Sun, G. Wang, Y. Cai, X. Gu, Z. Shuai and B. Z. Tang, Biradical-featured stable organic-small-molecule photothermal materials for highly efficient solar-driven water evaporation, *Adv. Mater.*, 2020, **32**, e1908537.
24 S. P. Prakoso, S. S. Sun, R. Saleh, Y. T. Tao and C. L. Wang, Tailoring photophysical properties of diketopyrrolopyrrole small molecules with electron-withdrawing moieties for efficient solar steam generation, *ACS Appl. Mater. Interfaces*, 2021, **13**, 38365–38374.
25 X. Zhang, Y. Li, Z. Chen, P. Li, R. Chen and X. Peng, Molecular engineering of narrow bandgap porphyrin derivatives for highly efficient photothermal conversion, *Dyes Pigm.*, 2021, **192**, 109460.
26 D. Wang, S. Qi, J. Dong, X. Wang, Y. Zhang, S. Zhou, P. Gu, T. Jia and Q. Zhang, D-A-type molecules with free rotors for highly efficient interfacial solar-driven steam generation and thermoelectric performance, *Org. Lett.*, 2023, **25**, 5730–5734.
27 J. Dai, S. Qi, M. Zhao, J. Liu, T. Jia, G. Liu, F. Liu, P. Sun, B. Li, C. Wang, J. Zhou and G. Lu, Donor-acceptor molecule with TICT character: A new design strategy for organic photothermal material in solar energy, *Chem. Eng. J.*, 2023, **471**, 144745.
28 K. Mebrouk, F. Chotard, C. L. Goff-Gaillard, Y. Arlot-Bonnemains, M. Fourmigue and F. Camerel, Water-soluble nickel-bis(dithiolene) complexes as photothermal agents, *Chem. Commun.*, 2015, **51**, 5268–5270.
29 M. Ciancone and F. Camerel, Laser triggered phase transition in photothermal liquid crystals, *Chem. Commun.*, 2017, **53**, 6339–6342.
30 B. Park, K. M. Lee, S. Park, M. Yun, H. J. Choi, J. Kim, C. Lee, H. Kim and C. Kim, Deep tissue photoacoustic imaging of nickel(II) dithiolene-containing polymeric nanoparticles in the second near-infrared window, *Theranostics*, 2020, **10**, 2509–2521.
31 K. Chen, W. Fang, Q. Zhang, X. Jiang, Y. Chen, W. Xu, Q. Shen, P. Sun and W. Huang, Tunable NIR absorption property of a dithiolene nickel complex: A promising NIR-II absorption material for photothermal therapy, *ACS Appl. Bio Mater.*, 2021, **4**, 4406–4412.
32 Y. Zhou, Q. Hu, F. Yu, G. Y. Ran, H. Y. Wang, N. D. Shepherd, D. M. D'Alessandro, M. Kurmoo and J. L. Zuo, A metal-organic framework based on a nickel bis(dithiolene) connector: Synthesis, crystal structure, and application as an electrochemical glucose sensor, *J. Am. Chem. Soc.*, 2020, **142**, 20313–20317.
33 B. Garreau-de Bonneval, K. I. Moineau-Chane Ching, F. Alary, T.-T. Bui and L. Valade, Neutral d^8 metal bis-dithiolene complexes: Synthesis, electronic properties and applications, *Coord. Chem. Rev.*, 2010, **254**, 1457–1467.
34 P. Deplano, L. Pilia, D. Espa, M. L. Mercuri and A. Serpe, Square-planar d^8 metal mixed-ligand dithiolene complexes as second order nonlinear optical chromophores: Structure/property relationship, *Coord. Chem. Rev.*, 2010, **254**, 1434–1447.
35 M. C. Aragoni, C. Caltagirone, V. Lippolis, E. Podda, A. M. Z. Slawin, J. D. Woollins, A. Pintus and M. Arca, Diradical character of neutral heteroleptic bis(1,2-dithiolene) metal complexes: Case study of [Pd(Me_2timdt)(mnt)] (Me_2timdt = 1,3-dimethyl-2,4,5-trithioxoimidazolidine; mnt^{2-} = 1,2-dicyano-1,2-ethylenedithiolate), *Inorg. Chem.*, 2020, **59**, 17385–17401.
36 A. Nakada, T. Matsumoto and H.-C. Chang, Redox-active ligands for chemical, electrochemical, and photochemical

molecular conversions, *Coord. Chem. Rev.*, 2022, **473**, 214804.

37 C. M. Amb, C. L. Heth, S. J. Evenson, K. I. Pokhodnya and S. C. Rasmussen, Thiophene-fused nickel dithiolenes: A synthetic scaffold for highly delocalized π-electron systems, *Inorg. Chem.*, 2016, **55**, 10978–10989.

38 B. Ding, M. B. Solomon, C. F. Leong and D. M. D'Alessandro, Redox-active ligands: Recent advances towards their incorporation into coordination polymers and metal-organic frameworks, *Coord. Chem. Rev.*, 2021, **439**, 213891.

39 C. Gates, H. Varnum, C. Getty, N. Loui, J. Chen, M. L. Kirk, J. Yang and S. J. Nieter Burgmayer, Protonation and non-innocent ligand behavior in pyranopterin dithiolene molybdenum complexes, *Inorg. Chem.*, 2022, **61**, 13728–13742.

40 Y. Cui, J. Liu, Z. Li, M. Ji, M. Zhao, M. Shen, X. Han, T. Jia, C. Li and Y. Wang, Donor–acceptor-type organic-small-molecule-based solar-energy-absorbing material for highly efficient water evaporation and thermoelectric power generation, *Adv. Funct. Mater.*, 2021, **31**, 2106247.

41 R. Zhang, N. Jin, T. Jia, L. Wang, J. Liu, M. Nan, S. Qi, S. Liu and Y. Pan, A narrow-bandgap photothermal material based on a donor–acceptor structure for the solar–thermal conversion application, *J. Mater. Chem. A*, 2023, **11**, 15380–15388.

42 H.-C. Li, H.-N. Li, L.-Y. Zou, Q. Li, P.-F. Chen, X.-N. Quan, K. Deng, C.-Q. Sheng, J. Ji, Q. Fan, Z.-K. Xu and J.-H. Wan, Vertically π-extended strong acceptor unit boosting near-infrared photothermal conversion of conjugated polymers toward highly efficient solar-driven water evaporation, *J. Mater. Chem. A*, 2023, **11**, 2933–2946.

43 K. Ray, T. Weyhermüller, F. Neese and K. Wieghardt, Electronic structure of square planar bis(benzene-1,2-dithiolato)metal complexes $[M(L)_2]^z$ (z = 2-, 1-, 0; M = Ni, Pd, Pt, Cu, Au): An experimental, density functional, and correlated *ab initio* study, *Inorg. Chem.*, 2005, **44**, 5345–5360.

44 M. Zha, X. Lin, J.-S. Ni, Y. Li, Y. Zhang, X. Zhang, L. Wang and K. Li, An ester-substituted semiconducting polymer with efficient nonradiative decay enhances NIR-II photoacoustic performance for monitoring of tumor growth, *Angew. Chem., Int. Ed.*, 2020, **59**, 23268–23276.

45 J.-S. Ni, X. Zhang, G. Yang, T. Kang, X. Lin, M. Zha, Y. Li, L. Wang and K. Li, A photoinduced nonadiabatic decay-guided molecular motor triggers effective photothermal conversion for cancer therapy, *Angew. Chem., Int. Ed.*, 2020, **59**, 11298–11302.

46 J.-S. Ni, P. Zhang, T. Jiang, Y. Chen, H. Su, D. Wang, Z.-Q. Yu, R. T. K. Kwok, Z. Zhao, J. W. Y. Lam and B. Z. Tang, Red/NIR-emissive benzo[*d*]imidazole-cored AIEgens: Facile molecular design for wavelength extending and *in vivo* tumor metabolic imaging, *Adv. Mater.*, 2018, **30**, 1805220.

47 J.-S. Ni and G.-H. Lu, Natural protoberberine alkaloid-montmorillonite nanocomposite powders with AIE features for visualizing high-resolution latent fingerprints, *Spectrochim. Acta, Part A*, 2023, **300**, 122908.

48 N. Arshad, I. Ahmed, M. S. Irshad, H. R. Li, X. Wang, S. Ahmad, M. Sharaf, M. Firdausi, M. Zaindin and M. Atif, Super hydrophilic activated carbon decorated nanopolymer foam for scalable, energy efficient photothermal steam generation, as an effective desalination system, *Nanomater*, 2020, **10**, 2510.

49 X. Liu, D. D. Mishra, X. Wang, H. Peng and C. Hu, Towards highly efficient solar-driven interfacial evaporation for desalination, *J. Mater. Chem. A*, 2020, **8**, 17907–17937.

50 M. J. Frisch, G. W. Trucks, H. B. Schlegel, G. E. Scuseria, M. A. Robb, J. R. Cheeseman, G. Scalmani, V. Barone, G. A. Petersson, X. L. H. Nakatsuji, M. Caricato, A. V. Marenich, J. Bloino, B. G. Janesko, R. Gomperts, B. Mennucci, H. P. Hratchian, J. V. Ortiz, A. F. Izmaylov, J. L. Sonnenberg, D. Williams-Young, F. Ding, F. Lipparini, F. Egidi, J. Goings, B. Peng, A. Petrone, D. R. T. Henderson, V. G. Zakrzewski, J. Gao, N. Rega, G. Zheng, W. Liang, M. Hada, M. Ehara, K. Toyota, R. Fukuda, J. Hasegawa, M. Ishida, T. Nakajima, Y. Honda, O. Kitao, H. Nakai, T. Vreven, K. Throssell, J. A. Montgomery Jr, J. E. Peralta, F. Ogliaro, M. J. Bearpark, J. J. Heyd, E. N. Brothers, K. N. Kudin, V. N. Staroverov, T. A. Keith, R. Kobayashi, J. Normand, K. Raghavachari, A. P. Rendell, J. C. Burant, S. S. Iyengar, J. Tomasi, M. Cossi, J. M. Millam, M. Klene, C. Adamo, R. Cammi, J. W. Ochterski, R. L. Martin, K. Morokuma, O. Farkas, J. B. Foresman and D. J. Fox, *Gaussian 16, Revision A.03*, Gaussian, inc., Wallingford CT, 2016.

